Journal of Magnetism and Magnetic Materials 482 (2019) 160–167

Contents lists available at ScienceDirect

Journal of Magnetism and Magnetic Materials

journal homepage: www.elsevier.com/locate/jmmm

Research articles

Structural, optical-vibration and magnetic properties of tetragonal lanthanide pyrogermanates obtained by molten-salt synthesis

Guilherme M. Martins[a], Silvana Mercone[b], Ricardo P.S.M. Lobo[c,d], Cristiano Fantini[e], Roberto L. Moreira[e], Anderson Dias[a,*]

[a] Departamento de Química, ICEx, Universidade Federal de Minas Gerais, C.P. 702, 31270-901 Belo Horizonte, MG, Brazil
[b] LSPM, CNRS UPR 3407, Université Paris 13, 99 Avenue J.-B. Clément, 93430 Villetaneuse, France
[c] LPEM, ESPCI Paris, PSL University, CNRS, F-75005 Paris, France
[d] Sorbonne Université, CNRS, LPEM, F-75005 Paris, France
[e] Departamento de Física, ICEx, Universidade Federal de Minas Gerais, C.P. 702, Belo Horizonte, MG 30123-970, Brazil

ARTICLE INFO

Keywords:
Ceramics
Raman spectroscopy
Magnetic properties
Pyrogermanates
Lanthanides
Spin ice

ABSTRACT

Lanthanide pyrogermanates of general formula $Ln_2Ge_2O_7$ (Ln = Tb, Dy, Ho, Er) were synthesized by molten-salt synthesis. Single-phase, impurity-free materials were obtained, which belong to the tetragonal $P4_12_12$ space group. Highly aggregated powders with good crystallinity were visualized by transmission electron microscopy techniques. Optical-vibration properties of the pyrogermanates were examined by Raman scattering. Lattice vibrations related to lanthanide ions presented upshifts due to decreasing lattice volumes (from Tb to Er), while Raman modes related to Ge-O vibrations remain unchanged or with little shift. $Dy_2Ge_2O_7$ clearly shows a peak in the *dc* magnetic susceptibility around 2.5 K under a relatively low applied field (paramagnetic to antiferromagnetic transition), while long-range magnetic ordering for the Tb-, Ho- and Er-containing ceramics could be observed down to 2 K. Curie-Weiss curves showed a higher Weiss temperature compared to literature in the case of $Tb_2Ge_2O_7$, suggesting a weak long-range order at low temperature, in the case of our sample. For the $Er_2Ge_2O_7$ compound, the presence of small Curie-Weiss temperatures reinforces the idea that antiferromagnetic and ferromagnetic dipolar exchange interactions between nearest neighbors compete at low temperature in our powders. All these features are coherent with a magnetic frustrated complex ground state such as the ones observed in the spin ices. Isothermal magnetization curves almost overlapped for the Dy, Ho and Tb compounds while it shows a sensitive non-standard behavior at low field in the case of the $Er_2Ge_2O_7$.

1. Introduction

Lanthanide (Ln) pyrogermanates ($Ln_2Ge_2O_7$) have attracted a rising interest since the early 1980s [1] owing to their chemical and physical properties, which can be used in different areas of modern engineering. More recently, the optical activity and the magnetic properties of $Ln_2Ge_2O_7$ materials highlighted a fascinating and diverse set of low-temperature magnetic states, from “spin liquid” to “spin glass” through “spin ice” behavior, which is a consequence of their geometrically frustrated lattice [2–8]. In this respect, these materials possess a variety of crystal structures: triclinic $P\bar{1}$ or $P1$ space groups (Ln = La-Gd), hexagonal $P6/mmm$ space group (Ln = Sm, Gd), tetragonal $P4_12_12$ space group (Ln = Gd-Lu), and high-temperature high-pressure cubic $Fd\bar{3}m$ pyrochlores [9–12]. The final structural arrangement depends on the ionic radius of the lanthanide as well as on the processing conditions, which in turn directly affect the final properties.

The first $Ln_2Ge_2O_7$ single crystals were obtained at the beginning of the 1970s, within the tetragonal structure, by Smolin (Yb, Er, Ho, Dy, Tb) [13] and Wanklyn (Tb-Lu) [14], using flux growth techniques. The work of Jouhet-Vetter and Queyroux [15] have revisited many compositions (belonging to three different structural groups) and presented the first manifestation of polymorphism in these materials. Bocquillon and Padiou [16] studied the polymorphism in $Sm_2Ge_2O_7$, showing that this material can be triclinic or hexagonal depending on the employed experimental conditions. The succeeding works reported structural determinations for $Gd_2Ge_2O_7$ and $Nd_2Ge_2O_7$ (both triclinic) [11,17], and $Eu_2Ge_2O_7$, $Tb_2Ge_2O_7$, $Er_2Ge_2O_7$, $Tm_2Ge_2O_7$ and $Lu_2Ge_2O_7$ (all with tetragonal structure) [3,13,18–21]. In 1987, Becker and Felsche published a complete crystal data for $Ln_2Ge_2O_7$ materials, in which La-Sm compounds are triclinic and the Eu-Lu analogous are tetragonal. Also, it

* Corresponding author.
E-mail address: andersondias@ufmg.br (A. Dias).

https://doi.org/10.1016/j.jmmm.2019.03.065
Received 6 December 2018; Received in revised form 5 February 2019; Accepted 13 March 2019
Available online 14 March 2019
0304-8853/

was verified polymorphism for Sm (triclinic or hexagonal), Eu (triclinic or tetragonal), and Gd (triclinic, hexagonal or tetragonal) materials; some of these materials revealed reversible structural phase transitions [11]. Completing the endeavor to understand the structural behavior of $Ln_2Ge_2O_7$ materials, cubic pyrochlore structures were also observed for high-temperature, high-pressure synthesized compounds in the early 1980s [1]. For these cubic structures, a huge amount of works was published in the last years concerning the low-temperature magnetic properties of both crystals and ceramics towards the understanding of their spin ice behavior [9,10,12,22–32]. Besides, Morosan et al. [30,31] studied the magnetothermodynamics of tetragonal $Dy_2Ge_2O_7$ and $Ho_2Ge_2O_7$ materials and their results expanded the initial believe that only cubic pyrochlore structures could exhibit *Ising*-like spins.

Concerning the vibrational properties of tetragonal $Ln_2Ge_2O_7$ materials, the report of Saez-Puche et al. [9] presents the Raman and infrared spectra only for the tetragonal $Y_2Ge_2O_7$. Previous studies, mentioned by Saez-Puche et al., investigated similar germanate compositions but with different crystalline structures [9]. This lack of information about the vibrational properties of these materials, recognized by Saez-Puche et al. and not elucidated so far, motivated us to conduct a detailed study on this subject, which can be useful for future investigations or applications. Thus, in the present work, four of the tetragonal lanthanide pyrogermanates (*Ln* = Tb, Dy, Ho and Er) were produced by molten-salt processing route. Structural, optical-vibration and *dc* magnetic investigations were conducted in all materials besides group-theory calculations. For the magnetic properties, Dy- and Ho-containing samples were used as references, since these tetragonal materials were previously studied by Morosan et al. [30,31]. The two new Tb- and Er-containing tetragonal pyrogermanates were investigated as promising anisotropic antiferromagnets. The purpose of this work is to show the correlation between crystal structure, phonon modes and the resulting magnetic properties for the tetragonal $Tb_2Ge_2O_7$, $Dy_2Ge_2O_7$, $Ho_2Ge_2O_7$, and $Er_2Ge_2O_7$ materials.

2. Experimental

$Ln_2Ge_2O_7$ (*Ln* = Tb, Dy, Ho, Er) powders were synthesized by molten-salt synthesis. Stoichiometric amounts of lanthanide oxides (Tb_4O_7, Dy_2O_3, Ho_2O_3, Er_2O_3) and GeO_2 (Sigma Aldrich, purity > 99.9%), according to the chemical reaction $Ln_2O_3 + 2GeO_2 = Ln_2Ge_2O_7$, were weighed, mixed and ground thoroughly by using acetone as fluid medium to ensure complete homogeneity. All lanthanides used in this work were heat treated at 900 °C overnight before being employed for the synthesis. The mixed powders were then calcined in a molten-salt flux of NaCl (Aldrich) at 900 °C, for 4 h, with intermediate regrinding (heating and cooling rates were 8 °C/min). After synthesis, the resulting products were washed in hot distilled water and diluted nitric acid (0.1 M) to dissolve and remove the residual NaCl and unreacted lanthanide oxides, followed by drying at 80 °C.

The crystalline structure of the samples was investigated by X-ray diffraction (XRD) by using a Shimadzu D-6000 diffractometer with graphite monochromator and a nickel filter in the range of 5–80°2θ (15 s/step of 0.02°2θ), operating with FeKα radiation (λ = 0.1936 nm), 40 kV and 20 mA. The results were automatically converted to CuKα radiation for data treatment and manipulation. The lattice parameters were determined by the software MDI Jade 9.0. Transmission electron microscopy (TEM) was employed to investigate both the morphology and the structure of the samples, using a Tecnai G2-20 (FEI) transmission microscope operating at 200 kV. The samples were dispersed in isopropanol and submitted to ultrasound (15 min) prior to be placed in holey carbon-copper grids (#300 mesh). High-resolution TEM (HRTEM), selected-area electron diffraction (SAED), convergent-beam electron diffraction (CBED), energy dispersive spectroscopy (EDS), and electron energy-loss spectroscopy (EELS) measurements were performed using the same Tecnai G2-10 instrument under 200 kV.

Micro-Raman spectroscopy was employed in backscattering configuration by using two equipments. First, it was used an Horiba LABRAM-HR spectrometer with the 632.8 nm line of a helium-neon laser as excitation source (effective power of 6 mW at the surface of each sample), diffraction gratings of 600 and 1800 grooves/mm, Peltier-cooled charge coupled device (CCD) detector, confocal Olympus microscope (100× objective), and experimental resolution of typically 1 cm^{-1} for 10 accumulations of 30 s in loose ceramic powders. In addition, it was used an Horiba T64000 triple monochromator (50× objective) equipped with the 568.2 nm line of a Kr^+ laser (effective power of 1 mW at the sample's surface) and a liquid-N_2-cooled charge coupled device (CCD) detector. The spectral resolution was better than 2 cm^{-1} and the accumulation times were typically 20 collections of 30 s in loose powders. All resulting spectra were corrected by Bose-Einstein thermal factor [33].

A Superconducting Quantum Interference Device (SQUID) also working as a Vibrational Standard Magnetometer (VSM) was used for the *dc* magnetization measurements. Magnetic *dc* susceptibilities were obtained as a function of the temperature from 2 K to 300 K, under different magnetic fields. *dc* susceptibilities have also been performed at low temperature (2 K and 3 K) for values of magnetic field up to 6 Tesla. Well-known density values for all the lanthanide compounds as well as a standard molecular model were used in order to obtain the appropriate magnetic unities. This allows comparing our results with the expected behavior in literature.

3. Results and discussion

XRD patterns for the ceramic powders are displayed in Fig. 1. The

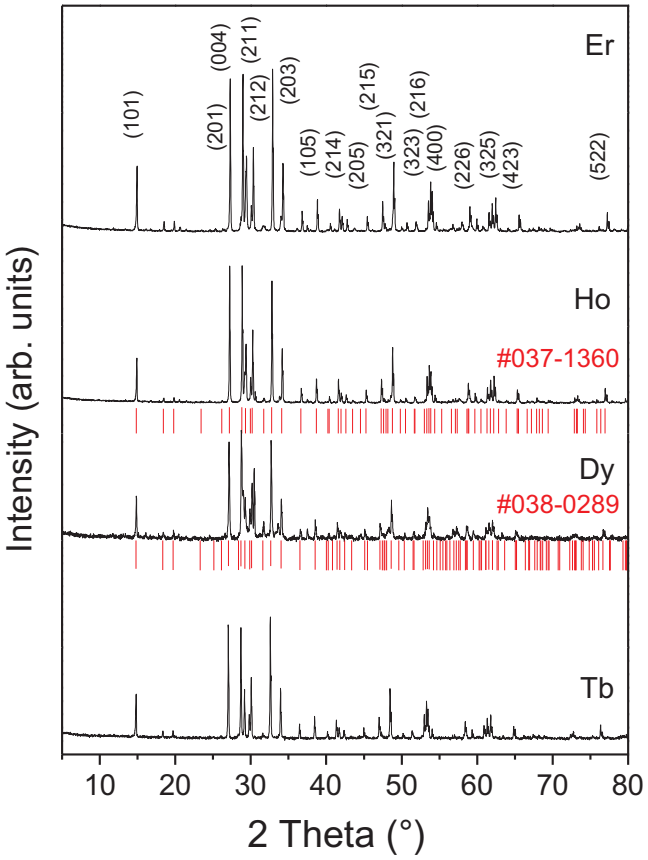

Fig. 1. Room-temperature XRD patterns with Miller indices for the Tb, Dy, Ho and Er pyrogermanates. Red lines show the standard patterns of these tetragonal compounds (JCPDS #38-0289 and #37-1360, for $Dy_2Ge_2O_7$ and $Ho_2Ge_2O_7$, respectively).

diffraction peaks can be indexed to phase-pure, tetragonal $Tb_2Ge_2O_7$, $Dy_2Ge_2O_7$, $Ho_2Ge_2O_7$ and $Er_2Ge_2O_7$ materials (Miller indices for the $P4_12_12$ space group are presented). The JCPDS files #00-38-0289 and #00-037-1360 were used as references for Dy- and Ho-containing samples, respectively. Diffraction peaks due to impurities corresponding to the starting materials were not observed in the patterns. The crystal structure was firstly described by Becker and Felsche [11], which is characterized by tetrahedral regular diortho-groupings of germanate ions $[Ge_2O_7]^{6-}$ and coordination number seven for the trivalent lanthanides Tb-Er; the coordination polyhedron is a pentagonal bipyramid [11,20]. The germanium atoms are tetrahedrally coordinated to oxygen, and pairs of each tetrahedra share corner oxygen ions to form $(Ge_2O_7)^{6-}$ entities that are isolated from each other [20]. For our samples, Fig. 1a exhibited a shift to higher diffraction angles from Tb to Er due to the decreasing ionic size for heavier lanthanides. The lattice parameters were then calculated for the $Ln_2Ge_2O_7$ samples by the equation:

$$\frac{1}{d^2} = \frac{h^2 + k^2}{a^2} + \frac{l^2}{c^2} \quad (1)$$

where a and c are the lattice parameters, d is the interplanar spacing, and h, k and l are the Miller indices. The experimental values were obtained for $Tb_2Ge_2O_7$ as $a = b = 6.867 \pm 0.005$ Å and $c = 12.458 \pm 0.008$ Å ($V = 587.47$ Å^3); while, for $Dy_2Ge_2O_7$, the lattice parameters were $a = b = 6.853 \pm 0.004$ Å and $c = 12.399 \pm 0.007$ Å ($V = 582.30$ Å^3). The heavier lanthanides Ho and Er exhibited experimental values for $a = b = 6.815 \pm 0.006$ Å, $c = 12.375 \pm 0.005$ Å, and $V = 574.75$ Å^3 ($Ho_2Ge_2O_7$); and lattice parameters of $a = b = 6.788 \pm 0.003$ Å, $c = 12.311 \pm 0.003$ Å and $V = 567.25$ Å^3, for $Er_2Ge_2O_7$.

The morphological, chemical and structural behaviors of the lanthanide pyrogermanates were examined by transmission electron microscopy. Fig. 2a presents the TEM images obtained for the $Tb_2Ge_2O_7$ ceramics synthesized at 900 °C. The morphology of the samples shows micrometer-sized particles formed by highly aggregated smaller particles (Fig. 2a, bottom inset). High-resolution image showed interplanar spacings of the order of 6.8 Å, which can be related to the (1 0 0) planes of the tetragonal $P4_12_12$ (#92) space group. The good crystallinity of the sample was verified by SAED (upper right inset in Fig. 2a), where the observed defined spots confirm the crystalline nature of the obtained materials. As an example, the interplanar spacing of the order of 2.7 Å, corresponding to the (2 1 2) planes, is showed. The upper left inset in Fig. 2a exhibits the convergent-beam electron diffraction (CBED) pattern of a selected area of about 50 nm in size. Instead of the diffraction spots that are obtained in the back focal plane of the objective lens with parallel illumination in conventional SAED, CBED produces discs of different intensities [34]. It is important to note that to determine the point group of our samples, a sufficient number of CBED patterns with the electron beam aligned along different zone axes was collected and manipulated. Then, the point group could be determined as the tetragonal $P4_12_12$ (#92), as expected, uniquely from the symmetry within the individual discs and the overall pattern. The positions of reflections in higher-order Laue zones were used to identify the crystal system and lattice type, and to detect the presence of glide planes [34,35]. Fig. 2b presents the EDS and EELS data for the $Tb_2Ge_2O_7$ sample, revealing both the valence electron (low-loss) peaks and the ionization edges of its fine structure. It was possible to observe and attribute many spectral features, corresponding to different excitation processes, thus emphasizing the high purity of our samples [36]. For the EELS data, after background subtraction, the experimental information was compared with reference (Ge and Tb_2O_3), which showed a significant shift in the energy related to the strong interaction between Ge and Tb in the $Tb_2Ge_2O_7$ compound.

Fig. 3a presents TEM images for the $Dy_2Ge_2O_7$ ceramics. Micrometer-sized rods were observed (upper inset) in the low-magnification image, while high-resolution images showed interplanar spacings of the order of 6.9 Å, 3.8 Å, and 2.7 Å, which correspond to the (1 0 0), (1 1 2), and (2 1 2) planes of the tetragonal $P4_12_12$ space group, respectively. Fig. 3b presents the EDS/EELS data for the $Dy_2Ge_2O_7$ ceramics, with their characteristic spectral features related to the different excitation process occurring in this high-purity sample. EELS data are presented after background subtraction and with a pertinent comparison with the references Ge and Dy_2O_3. The results showed an expected shift in energy, which is related to the strong interaction between Ge and Dy in $Dy_2Ge_2O_7$ ceramics. SAED pattern is presented in Fig. 3c (upper right image), where random well-defined spots are observed, which confirms the crystalline nature of the obtained materials. For this sample, in order to better understand the result without rotating and tilting the specimen, we use a profile generator [37], after carefully finding the center of the SAED pattern displayed in Fig. 3c (upper image). The results allowed us to obtain precise peak positions, which could be indexed by the different crystallographic planes of the tetragonal $P4_12_12$ structure (see Fig. 3c).

Fig. 4a exhibits TEM images for the $Ho_2Ge_2O_7$ compounds. Micrometer-sized particles were observed (left upper inset) in the low-magnification image, while HRTEM images showed interplanar spacings of the order of 6.7 Å and 3.1 Å, which are related to the (1 0 0) and (0 0 4) planes of the tetragonal $P4_12_12$ structure, respectively. Fig. 4b shows the EDS/EELS data for the $Ho_2Ge_2O_7$ samples, which represent their main excitation processes within the sample here visualized as spectral signatures in this high-purity sample. The results for EELS are showed after background subtraction and comparison with the references Ge and Ho_2O_3. A shift in energy was observed, as previously discussed, and corresponds to the interactions between Ge and Ho ions in the $Ho_2Ge_2O_7$ materials. A SAED pattern is presented in Fig. 4c (upper right image), where randomly oriented spots are observed. Again, in order to improve the understanding without rotating and tilting the specimen, it was used a profile generator after carefully finding the center of the SAED pattern displayed in Fig. 4c. The precise peak positions were obtained and were then indexed according to the crystallographic planes expected for the tetragonal $P4_12_12$ space group (Fig. 4c).

The results of the TEM measurements for the $Er_2Ge_2O_7$ ceramics are displayed in Fig. 5. The right upper inset in Fig. 5a presents a low-magnification image for this sample, where micrometer-sized particles can be visualized. HRTEM images show interplanar spacings of the order of 5.9 Å, 4.4 Å, and 3.1 Å, which are related to the (1 0 1), (1 1 1) and (1 0 0) planes of the tetragonal $P4_12_12$ structure, respectively. SAED pattern is showed in the left upper inset, which confirms the high crystallinity of the sample and its well-aligned nature. Fig. 5b shows the EDS/EELS data for the $Er_2Ge_2O_7$ materials, which exhibit the usual spectral features related to the associated excitation processes. The results for EELS showed a shift in energy if compared with reference data, as verified for the other samples and discussed above.

Fig. 6 presents the Raman spectra for the $Ln_2Ge_2O_7$ powders obtained by molten-salt method at 900 °C. The spectra show a series of bands in the wavenumber range 150–900 cm^{-1}, consistent with the tetragonal $P4_12_12$ (#92) space group obtained in the present work, as discussed below. According to Saez-Puche et al. [9], the wavenumber range 700–900 cm^{-1} corresponds to the GeO_3 symmetric and asymmetric stretching modes, while the intermediate wavenumber range (350–700 cm^{-1}) is related to the deformational GeO_3 and stretching Ge-O-Ge modes. Bands below 350 cm^{-1} are due to the lattice vibrations [9]. Spectra taken at several spots throughout the samples are identical, which indicate that the samples are single-phase, in agreement with the results of XRD and TEM analyses. The overall spectra response of all materials is similar. The absence of Raman spectra of these materials in the literature difficults the comparison with our results. However, based in our previous experience with similar samples replacing lanthanides ions [38–45], it is possible to explain the small differences observed in Fig. 6. First of all, the lanthanides investigated present very small differences in their ionic radii (Tb > Dy > Ho > Er). Thus, lattice vibrations related to these ions tend to change their wavenumbers due to

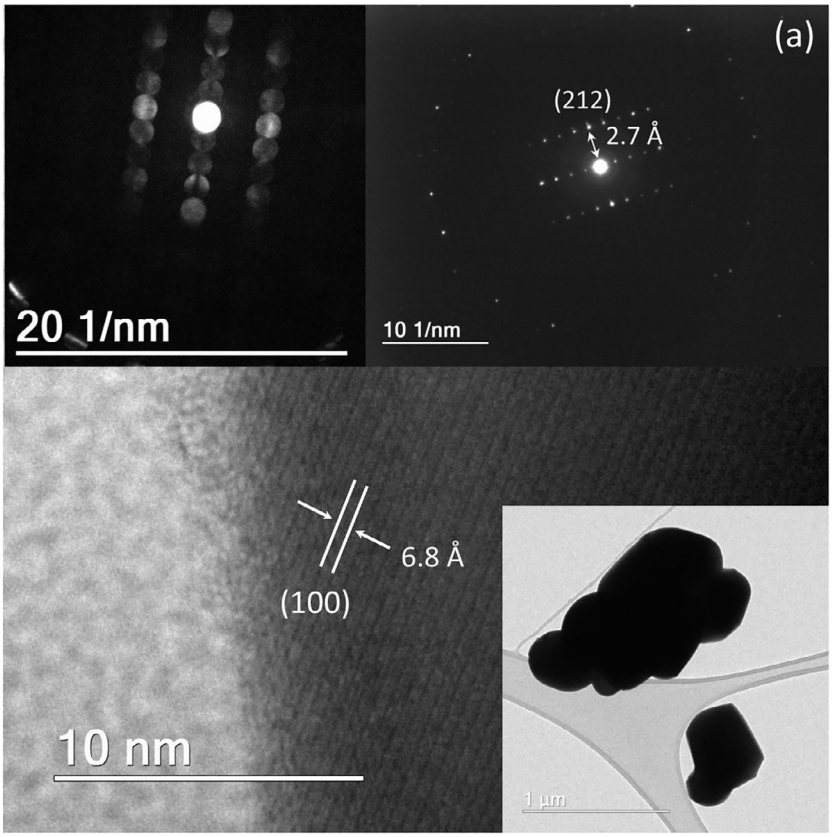

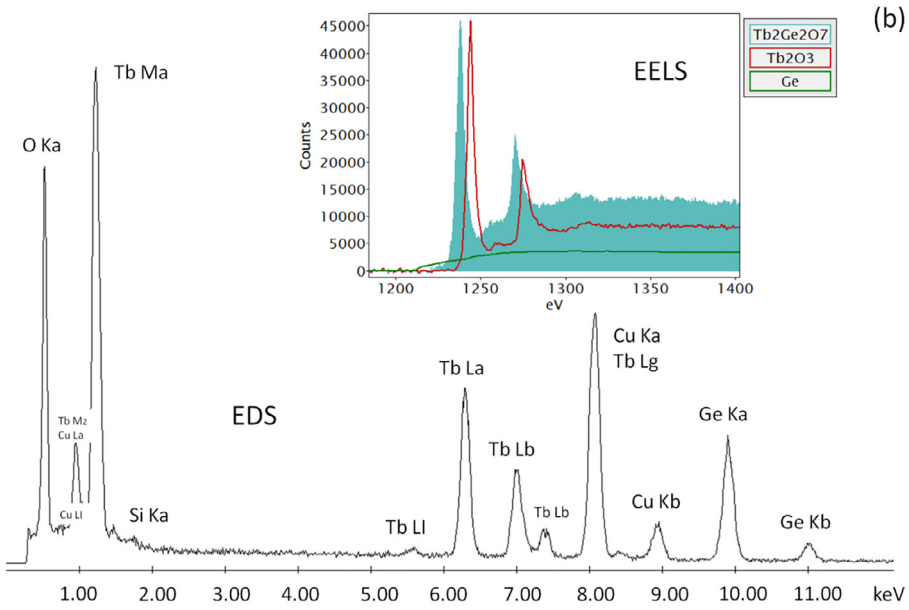

Fig. 2. (a) TEM/HRTEM images, SAED and CBED patterns for the $Tb_2Ge_2O_7$ ceramics obtained at 900 °C. The bottom inset exhibits the morphology in a low-magnification image, while the HRTEM image shows the interplanar spacing for the (1 0 0) planes of the tetragonal $P4_12_12$ (#92) structure. The SAED pattern is shown in the right upper inset, evidencing the crystalline nature of the compounds (the interplanar spacing corresponding to the (2 1 2) planes is also shown). CBED pattern (left upper inset) confirms the tetragonal space group for this sample. (b) EDS/EELS spectra for the $Tb_2Ge_2O_7$ ceramics, where the electronic energies of all ions present into the structure were clearly identified.

the high sensitivity of these phonon modes with the volume of the unit cell (upshifts are expected for smaller lattice volumes). Many bands remain unchanged or with little shift, which could be an indication of Ge-related vibrations. Beside, terbium is lighter than erbium (158.93 g/mol against 167.26 g/mol), which contributes with a softening of modes strongly sensitive to the molar mass, in an opposite sense that given by the lanthanide contraction.

For $Ln_2Ge_2O_7$ ceramics, the tetragonal structure ($P4_12_12$ space group, #92) contains 11 atoms in its primitive cell. *Ln* and Ge atoms occupy 8*b*-Wyckoff sites, while four inequivalent special sites (4*a* and 8*b*) are occupied by oxygen anions. Factor group analysis (Table 1) yields $16A_1 + 17B_1 + 16B_2 + 32E$ Raman-active, and $16A_2 + 32E$ infrared-active vibrational modes (in addition to the $A_2 + E$ acoustic phonons). Table 2 shows the phonon positions obtained through a least squares fitting of the data to a series of Lorentzian peaks (not shown). We identified 26 Raman modes in each sample (see in Fig. 6 a labeled spectrum). Table 2 shows that a gradual increase for higher frequencies (upshifts with increasing *Ln* atomic number) is observed for practically all bands, which is an exclusive consequence of the lanthanide contraction. We believe that the experimental results reported in the

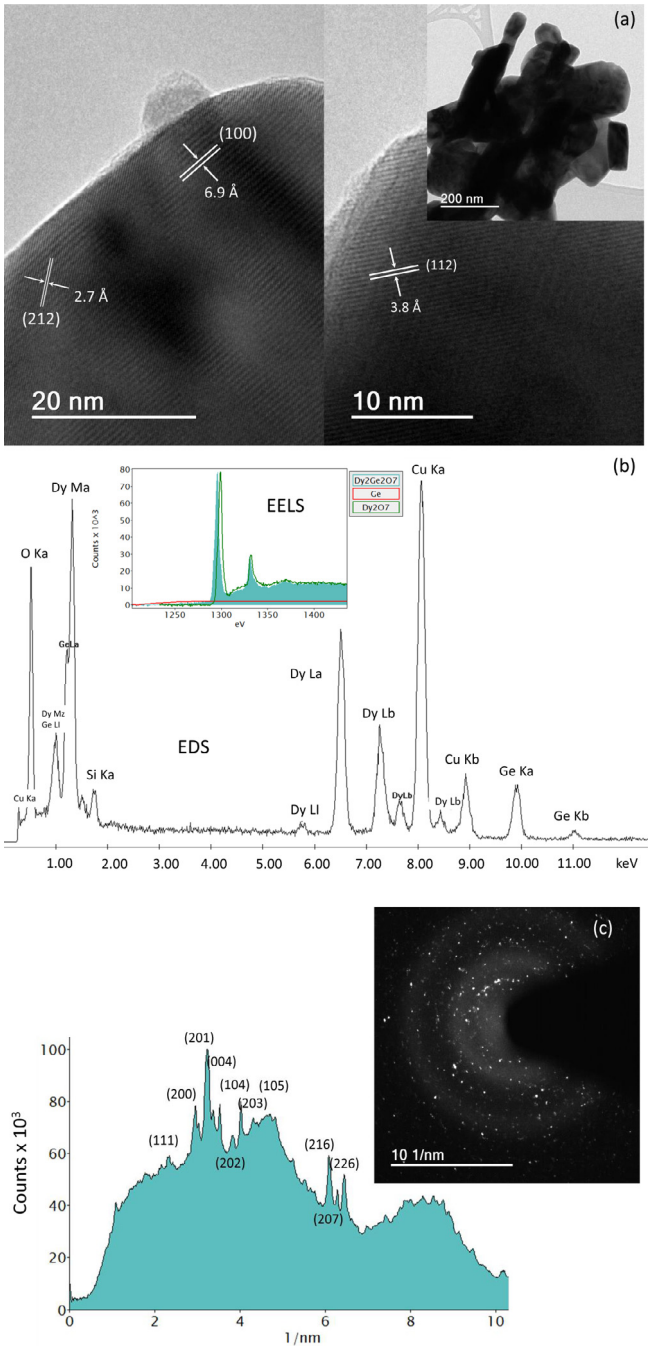

Fig. 3. (a) TEM/HRTEM images for the $Dy_2Ge_2O_7$ ceramics. The upper inset exhibits the morphology in a low-magnification image, while the HRTEM images show the interplanar spacing for the (1 0 0), (1 1 2), and (2 1 2) planes of the tetragonal $P4_12_12$ space group. (b) EDS/EELS spectra for the $Dy_2Ge_2O_7$ ceramics with all the electron energies clearly identified. (c) SAED pattern (upper image) and corresponding profile for the observed random spots, evidencing the crystalline nature of the sample (some crystallographic planes are indicated).

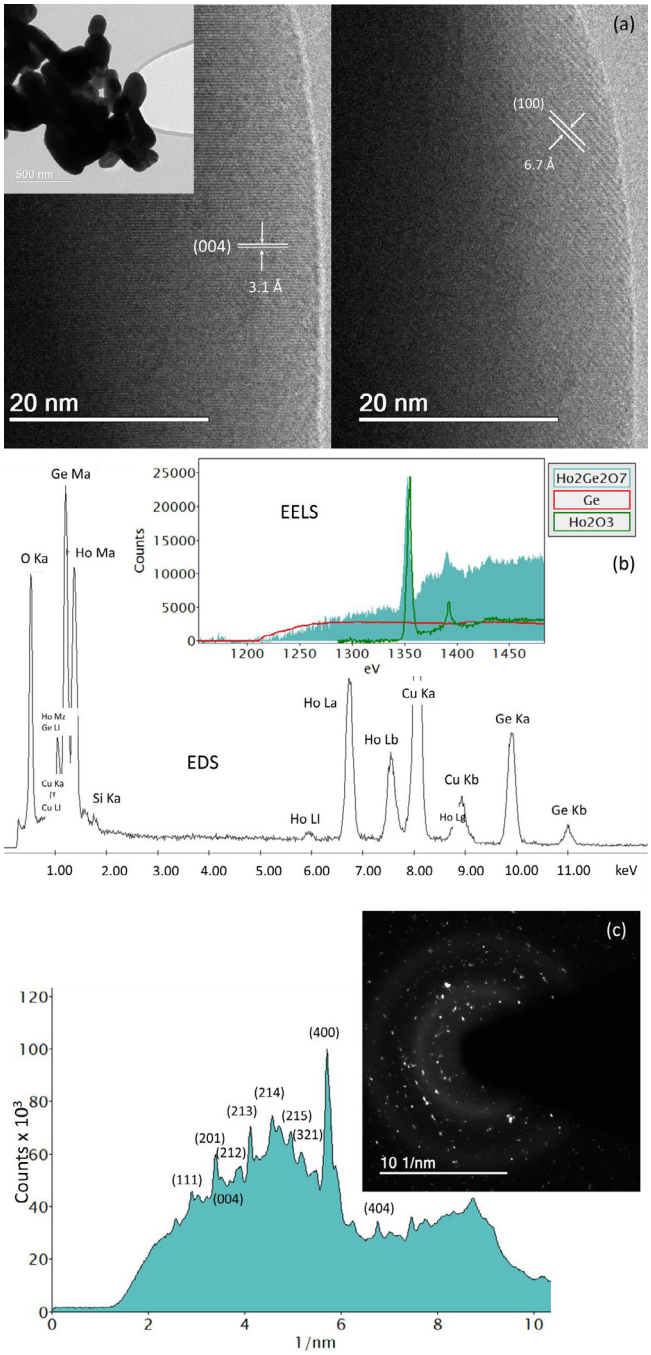

Fig. 4. (a) TEM/HRTEM images for the $Ho_2Ge_2O_7$ materials. The left upper inset exhibits the morphological features in low magnification, while HRTEM images show the interplanar spacing for the (1 0 0) and (0 0 4) planes of the tetragonal $P4_12_12$ space group. (b) EDS/EELS spectra for the $Ho_2Ge_2O_7$ ceramics with the electronic energies identified. (c) SAED pattern (right upper image) and corresponding SAED profile for the randomly oriented spots observed (relevant crystallographic planes are marked).

present work give useful information for describing the vibrational properties of these materials, which can help to enhance the understanding of other properties from the fundamental point of view and for application purposes.

At this point, we shall analyze the magnetic properties of our tetragonal $Ln_2Ge_2O_7$ materials. Fig. 7 shows the temperature dependence of the *dc* susceptibility (M/H) for all samples at 0.01 and 0.1 T (0.2 for Dy) above 2 K. The insets report the high temperature behavior of the inverse of the measured susceptibility (H/M) in order to show their linear Curie-Weiss behavior. These results point out that, while the $Dy_2Ge_2O_7$ shows a peak in the *dc* susceptibility around 2.5 K under a relatively low applied field; for all the other cases (Tb-, Ho- and Er-containing materials) this peak could not be observed in the measured temperature ranges. In the measured range, *dc* susceptibility shows no sign of long range magnetic ordering for the Tb-, Ho- and Er-containing powders. In the case of the $Dy_2Ge_2O_7$, the peak agrees with the literature [30] as it broadens and moves to lower temperatures with the

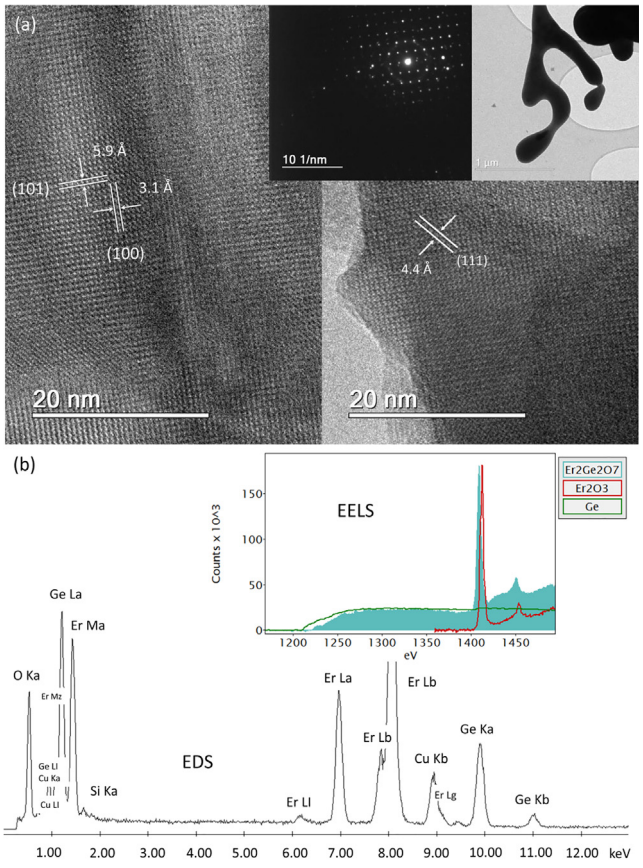

Fig. 5. (a) TEM/HRTEM images and SAED pattern for the $Er_2Ge_2O_7$ materials. The right upper inset exhibits the morphological features in a low-magnification image, while HRTEM images show the interplanar spacing for the (1 0 1), (1 1 1) and (1 0 0) planes of the tetragonal $P4_12_12$ space group. SAED pattern (left upper inset) shows well-crystallized, aligned samples. (b) EDS/EELS spectra for the $Er_2Ge_2O_7$ ceramics with the electronic energies identified, and reference data presented for comparison purposes.

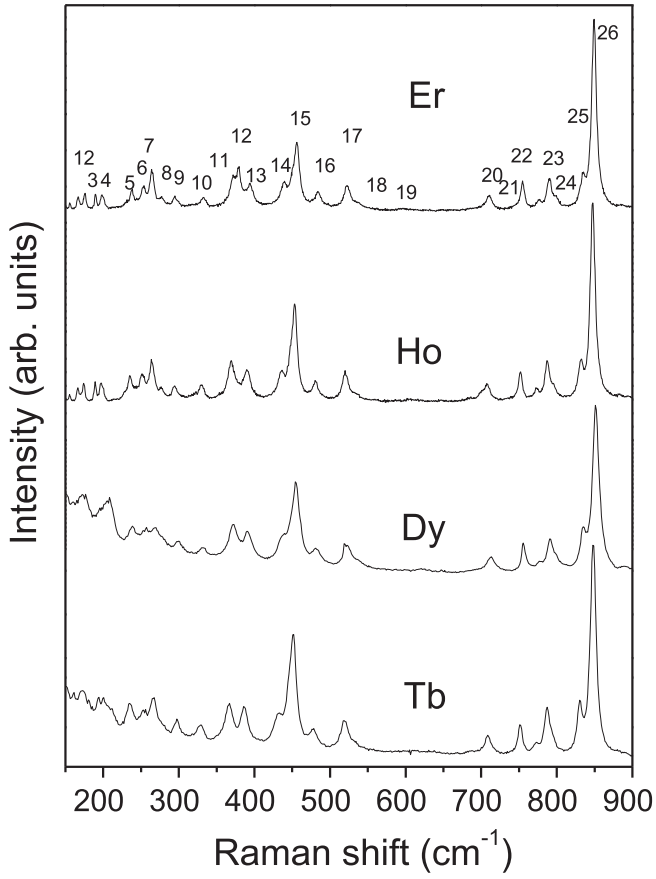

Fig. 6. Raman spectra for the $Ln_2Ge_2O_7$ compounds in the wavenumber region 150–900 cm^{-1}.

Table 1
Factor-group analysis for the $Ln_2Ge_2O_7$ (Ln = Tb-Er) compounds with tetragonal ($P4_12_12$, #92, D_4^4) structure (Z = 4).

Atom	Wyckoff sites	Symmetry	Irreducible representations
Ln	8*b*	C_1	$3A_1 + 3A_2 + 3B_1 + 3B_2 + 6E$
Ge	8*b*	C_1	$3A_1 + 3A_2 + 3B_1 + 3B_2 + 6E$
$O_{(1)}$	4*a*	C_2'	$A_1 + 2A_2 + 2B_1 + 1B_2 + 3E$
$O_{(2)}$	8*b*	C_1	$3A_1 + 3A_2 + 3B_1 + 3B_2 + 6E$
$O_{(3)}$	8*b*	C_1	$3A_1 + 3A_2 + 3B_1 + 3B_2 + 6E$
$O_{(4)}$	8*b*	C_1	$3A_1 + 3A_2 + 3B_1 + 3B_2 + 6E$

$\Gamma_{TOTAL} = 16A_1 + 17A_2 + 17B_1 + 16B_2 + 33E$, $\Gamma_{ACOUSTIC} = A_2 + E$
$\Gamma_{RAMAN} = 16A_1 + 17B_1 + 16B_2 + 32E$ and $\Gamma_{INFRARED} = 16A_2 + 32E$

increasing field. Both the zero-field-cooled and field-cooled susceptibilities are the same (not shown) for all the compounds studied here. Our $Dy_2Ge_2O_7$ sample presents a magnetic behavior that is coherent with the previous results (crystal and ceramic samples) [30] and consistent with the presence of a paramagnetic (PM) to a long-range-ordered antiferromagnetic (AFM) state at very low temperature. In fact, while the external magnetic field increases the Zeeman energy, it also competes with the AFM exchange energy. This competition first broadens the long-range order peak, and eventually suppresses it, which is coherent with the observations in Fig. 7 for $Dy_2Ge_2O_7$.

Based on the *dc* susceptibility of Fig. 7 and previous works [30,31], we argue that the four compositions have similar magnetic properties, suggesting the existence of a magnetic order at very low temperature ($T < 2$ K) also in the case of Tb, Ho and Er powders. Indeed, the Curie-Weiss law fits (insets in Fig. 7) well the inverse susceptibility measured in different fields. We found positive Weiss temperatures very close to zero (see Table 3), and in agreement with published values for $Dy_2Ge_2O_7$ and $Ho_2Ge_2O_7$ [30,31]. We obtained a higher Weiss temperature compared to literature in the case of $Tb_2Ge_2O_7$ [26] and $Er_2Ge_2O_7$ [46], suggesting a weak long order at low temperature in the case of our sample. It is important to underline that the absolute value of the Weiss temperature can be affected by the temperature cutoff used for the analysis. In our case we analyzed the inverse of the susceptibility in a lower range of temperature then the one found in literature. This cannot in any circumstances explain the difference of quite 14 K observed for our $Er_2Ge_2O_7$ sample (Weiss temperature from Taddei et al. [46] is −14 K). The presence of close-to-zero Curie-Weiss temperatures reinforces the idea that AFM and ferromagnetic dipolar exchange interactions between nearest neighbors compete at low temperature in our powders. All these features are coherent with a magnetic frustrated scenario of a complex ground state as the spin ices ones.

In Fig. 8a, we present measurements of the isothermal magnetization as function of applied field at 2 K (Dy, Ho and Tb) and 3 K (Er). Interestingly, the isothermal curves almost overlapped for the Dy, Ho and Tb compounds while it shows a sensitive non-standard behavior at low field in the case of the $Er_2Ge_2O_7$. We report in Table 3 the magnetization at saturation experimentally obtained by the isothermal curves in Fig. 8a and we put them in graph as function of the atomic number of the lanthanides in Fig. 8b. They are all comparable with the effective value reported from literature on the base of a standard Ln^{3+} free-ion molecular model (*Ln* = Tb, Dy, Ho, Er). Lower magnetic moment in respect to the theoretical expected values have already been observed in the in the case of $Dy_2Ge_2O_7$ single crystal samples as well as

Table 2
Phonon wavenumbers (cm^{-1}) obtained from the Raman experimental data for the investigated tetragonal $Ln_2Ge_2O_7$ ceramics.

Band	$Ln_2Ge_2O_7$ (Wavenumber, cm^{-1})			
#	Tb	Dy	Ho	Er
1	171.3	171.6	172.2	172.4
2	179.4	180.2	181.1	182.5
3	193.2	194.0	195.2	195.9
4	202.9	203.7	204.5	205.8
5	233.0	235.3	238.3	242.4
6	253.5	255.3	256.8	259.3
7	267.8	268.6	269.6	270.1
8	277.1	279.2	280.4	282.5
9	298.7	299.4	300.6	301.8
10	329.3	331.6	333.4	335.8
11	366.5	369.7	372.1	374.6
12	385.5	387.4	389.7	391.2
13	399.0	401.2	403.6	405.3
14	432.1	436.3	439.6	443.4
15	450.1	452.9	454.8	457.4
16	477.0	480.3	483.5	487.6
17	519.8	521.9	524.6	527.9
18	563.3	565.4	566.8	567.9
19	594.5	595.8	596.7	597.4
20	708.0	710.5	713.6	716.7
21	751.5	754.8	757.9	760.5
22	772.1	774.3	776.4	778.7
23	788.1	790.4	793.6	795.8
24	796.0	799.2	802.4	805.2
25	831.6	834.4	837.7	840.2
26	849.0	851.2	853.0	854.8

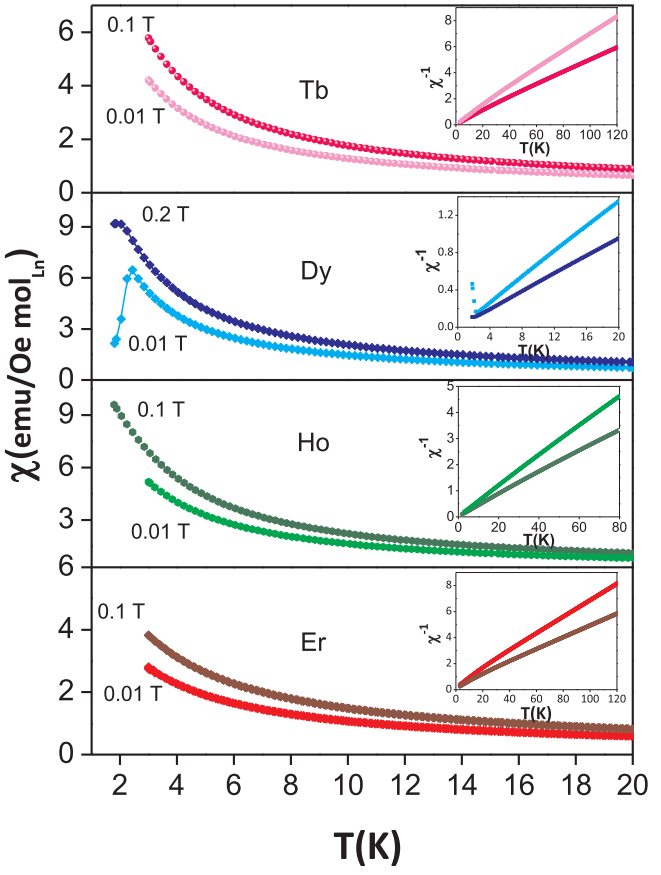

Fig. 7. Temperature dependence of the *dc* susceptibility of the $Ln_2Ge_2O_7$ powder samples (where *Ln* = Tb, Dy, Ho, Er) with different applied magnetic field. Insets show the expanded view of the inverse dc susceptibility as function of temperature and the Curie-Weiss fit.

Table 3
Comparison of the Curie-Weiss temperatures obtained by the linear fit of the χ^{-1} (see inset in Fig. 7) at high temperature, and the experimental values of magnetization at saturation (M_{sat}). μ_{eff} values are also reported from the literature.

Sample	θ_{CW} (K)	M_{Sat} (μ_B/f.u.)	μ_{eff} (μ_B/f.u.)
$Tb_2Ge_2O_7$	0.19 ± 0.01	8.6 ± 0.4	9.87 ± 0.03
$Dy_2Ge_2O_7$	0.02 ± 0.01	9.1 ± 0.5	10.5 ± 0.1
$Ho_2Ge_2O_7$	0.14 ± 0.01	10.3 ± 0.5	10.2 ± 0.1
$Er_2Ge_2O_7$	0.482 ± 0.002	9.2 ± 0.5	9.8 ± 0.3

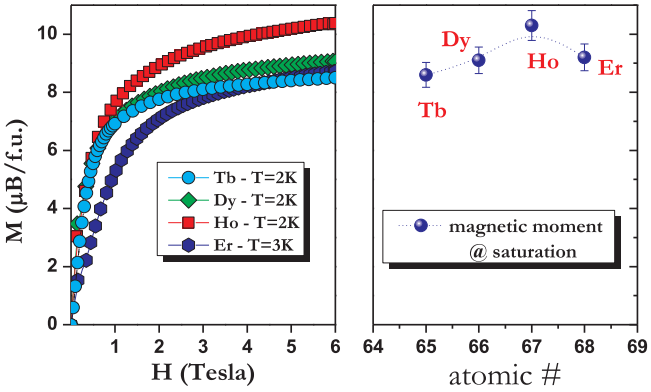

Fig. 8. (a) Field dependence of magnetization of the four powder samples at low temperature (T = 2–3 K); (b) Experimental magnetization at saturation obtained from the graph in (a) as function of the atomic number of the lanthanide atoms.

in the $Ho_2Ge_2O_7$ powders and has been attributed to a loss of the full moment due either to an *Ising*-like doublet ground state and/or the presence of a strong crystal electric field (CEF) [30,31].

4. Conclusions

Single-phase, impurity-free $Ln_2Ge_2O_7$ (*Ln* = Tb, Dy, Ho, Er) materials belonging to the tetragonal $P4_12_12$ space group were synthesized by molten-salt synthesis. Micrometer-sized particles formed by highly aggregated smaller particles with good crystallinity were visualized by TEM techniques (HR images and CBED patterns). The Raman spectra of these pyrogermanates showed a large number of phonons, well consistent with the tetragonal $P4_12_12$ (#92) space group. For all materials, 26 Raman bands were depicted in the spectral range 150–900 cm^{-1}. Lattice vibrations related to lanthanide ions presented upshifts due to smaller lattice volumes (from Tb to Er), while Raman modes related to Ge-O vibrations remain unchanged or with little shift. At low temperatures, $Dy_2Ge_2O_7$ shows a PM-to-AFM transition around 2.5 K, while long-range magnetic ordering for the Tb-, Ho- and Er-germanate ceramics was observed. Curie-Weiss curves showed a higher Weiss temperature compared to the literature in the case of $Tb_2Ge_2O_7$, suggesting a weaker long-range order at low temperature in the case of our sample. For $Er_2Ge_2O_7$ compound, the presence of small Curie-Weiss temperatures reinforces the idea that AFM exchange interactions and FM dipolar ones between nearest neighbors are in competition at low temperature in our powders. All these features are coherent with a magnetic frustrated scenario of a complex ground state as the spin ices ones. Isothermal magnetization curves almost overlapped for the Dy, Ho and Tb compounds, while it shows a sensitive non-standard behavior at low field in the case of the $Er_2Ge_2O_7$. Differences observed in the static magnetic behavior (*i.e.* Curie Weiss temperatures and/or magnetization at saturation) compared to the expectations in these pyrogermanates ceramics open interesting questions on the existence of the *Ising*-like doublet ground state and/or anisotropy as well as the presence

of a strong crystal electric field.

Acknowledgements

The authors acknowledge the financial support from Conselho Nacional de Desenvolvimento Científico e Tecnológico-CNPq, Coordenação de Aperfeiçoamento de Pessoal do Ensino Superior-CAPES and Fundação de Amparo à Pesquisa do Estado de Minas Gerais-FAPEMIG. The Center of Microscopy at the Universidade Federal de Minas Gerais (http://www.microscopia.ufmg.br) is also acknowledged for providing the equipment and technical support for experiments involving electron microscopy. The entire staff of the MPBT (physical properties – low temperature) platform of Sorbonne University is kindly acknowledged for their support. The work on the magnetic measurements at LPEM was supported by a grant from Région Île-de France.

Appendix A. Supplementary data

Supplementary data to this article can be found online at https://doi.org/10.1016/j.jmmm.2019.03.065.

References

[1] L.N. Demianets, A.N. Lobachev, G.A. Emelchenko, Rare-earth germanates, in: H.C. Freyhardt (Ed.), Crystals: growth, properties, and applications. 4. Organic crystals, Germanates, Semiconductors, Springer, Berlin Heidelberg, 1980, pp. 101–144.
[2] B. Karmakar, D. Nath, M. Chowdhury, M. Vala, Lanthanide chirality as a tool for assignment of transitions: Tm^{3+} and Tb^{3+} pyrogermanates, Spectrochim. Acta 42A (1986) 1193–1195.
[3] K. Stadnika, A.M. Glazer, M. Koralewski, B.M. Wanklyn, Structure and absolute optical chirality of thulium pyrogermanate crystals, J. Phys.: Condens. Matter 2 (1990) 4795–4805.
[4] K. Das, S. Jana, D. Ghosh, B.M. Wanklyn, Study of optical absorption spectra and magnetic susceptibilities of Tm^{3+}-pyrogermanate ($Tm_2Ge_2O_7$), J. Magn. Magn. Mater. 189 (1998) 310–320.
[5] J.S. Gardner, M.J. Gingras, J.E. Greedan, Magnetic pyrochlore oxides, Rev. Mod. Phys. 82 (2010) 53–107.
[6] C. Lacroix, P. Mendels, F. Mila, Introduction to Frustrated Magnetism: Materials, Experiments, Theory, Springer Series in Solid-State Sciences 164, Springer, Berlin Heidelberg, 2011.
[7] T. Fennell, Neutron scattering studies of spin ices and spin liquids, Collection SFN 13 (2014) 04001.
[8] L.D.C. Jaubert, J.T. Chalker, P.C.W. Holdsworth, R. Moessner, Spin ice under pressure: symmetry enhancement and infinite order multicriticality, Phys. Rev. Lett. 105 (2010) 082701.
[9] R. Saez-Puche, M. Bijkerk, F. Fernandez, E.J. Baran, I.L. Botto, Crystallographic data, vibrational spectra and magnetic properties of the lanthanide digermanates $Ln_2Ge_2O_7$, J. Solid State Chem. 184 (1992) 25–34.
[10] H.Y. Playford, C.L. Bull, M.G. Tucker, N.P. Funnell, C.J. Ridley, K.P. Marshallc, R.I. Walton, In situ neutron diffraction study of the formation of $Ho_2Ge_2O_7$ pyrochlore at high temperature and pressure, Dalton Trans. 46 (2017) 15415–15423.
[11] U.W. Becker, J. Felsche, Phases and structural relations of the rare earth germanates $RE_2Ge_2O_7$, RE≡ La-Lu, J. Less-Common Metals 128 (1987) 269–280.
[12] A.M. Hallas, J.A.M. Paddison, H.J. Silverstein, A.L. Goodwin, J.R. Stewart, A.R. Wildes, J.G. Cheng, J.S. Zhou, J.B. Goodenough, E.S. Choi, G. Ehlers, J.S. Gardner, C.R. Wiebe, H.D. Zhou, Statics and dynamics of the highly correlated spin ice $Ho_2Ge_2O_7$, Phys. Rev. B 86 (2012) 134431.
[13] Y.I. Smolin, Determination of the crystal structure of erbium pyrogermanate, $Er_2Ge_2O_7$, Sov. Phys. Crystallogr. 15 (1970) 36–39.
[14] B.M. Wanklyn, Flux growth of the rare earth germanates, J. Mater. Sci. 8 (1973) 649–653.
[15] G. Jouhet-Vetter, F. Queyroux, Study of some $Ln_2Ge_2O_7$ compounds (Ln= La, Nd, Sm, Eu, Gd), Mater. Res. Bull. 10 (1975) 1201–1204.
[16] G. Bocquillon, J. Padiou, Polymorphisme sous pression de $Sm_2Ge_2O_7$ et identification de la nouvelle phase H de la serie des digermanates de terres rares, Mater. Res. Bull. 15 (1980) 1069–1072.
[17] Y.I. Smolin, Y.I. Shepelev, I.K. Butikova, Determination of the crystal structure of gadolinium germanate (IV), Kristallografiya 16 (1971) 911–917.
[18] G. Vetter, F. Queyroux, P. Labbe, M. Goreaud, Détermination structurale de $Nd_2Ge_2O_7$, J. Solid State Chem. 45 (1982) 293–302.
[19] M.I. Chiragov, KhS. Mamedov, T.Z. Kulieva, Yttrium pyrogermanate, $Y_2Ge_2O_7$, Sov. Phys. Crystallogr. 28 (1983) 613-613.
[20] S. Geller, J.M. Gaines, The crystal structure of terbium pyrogermanate, $Tb_2Ge_2O_7$, Z. Kristallogr. 180 (1987) 243–247.
[21] K.K. Palinka, N.E. Kuz'mina, B.F. Dzhurinskii, Lutetium digermanate $Lu_2Ge_2O_7$, Zh, Neorg. Khim. 40 (1995) 1449–1451.
[22] H.D. Zhou, S.T. Bramwell, J.G. Cheng, C.R. Wiebe, G. Li, L. Balicas, J.A. Bloxsom, H.J. Silverstein, J.S. Zhou, J.B. Goodenough, J.S. Gardner, High pressure route to generate magnetic monopole dimers in spin ice, Nature Commun. 2 (2001) 478.
[23] H.D. Zhou, J.G. Cheng, A.M. Hallas, C.R. Wiebe, G. Li, L. Balicas, J.S. Zhou, J.B. Goodenough, J.S. Gardner, E.S. Choi, Chemical pressure effects on pyrochlore spin ice, Phys. Rev. Lett. 108 (2012) 207206.
[24] X. Li, W.M. Li, K. Matsubayashi, Y. Sato, C.Q. Jin, Y. Uwatoko, T. Kawae, A.M. Hallas, C.R. Wiebe, A.M. Arevalo-Lopez, J.P. Attfield, J.S. Gardner, R.S. Freitas, H.D. Zhou, J.-G. Cheng, Long-range antiferromagnetic order in the frustrated XY pyrochlore antiferromagnet $Er_2Ge_2O_7$, Phys. Rev. B 89 (2014) 064409.
[25] Z.L. Dun, M. Lee, E.S. Choi, A.M. Hallas, C.R. Wiebe, J.S. Gardner, E. Arrighi, R.S. Freitas, A.M. Arevalo-Lopez, J.P. Attfield, H.D. Zhou, J.-G. Cheng, Chemical pressure effects on magnetism in the quantum spin liquid candidates $Yb_2X_2O_7$ (X= Sn, Ti, Ge), Phys. Rev. B 89 (2014) 064401.
[26] A.M. Hallas, J.-G. Cheng, A.M. Arevalo-Lopez, H.J. Silverstein, Y. Su, P.M. Sarte, H.D. Zhou, E.S. Choi, J.P. Attfield, G.M. Luke, C.R. Wiebe, Incipient ferromagnetism in $Tb_2Ge_2O_7$: application of chemical pressure to the enigmatic spin-liquid compound $Tb_2Ti_2O_7$, Phys. Rev. Lett. 113 (2014) 267205.
[27] Z.L. Dun, X. Li, R.S. Freitas, E. Arrighi, C.R. Dela Cruz, M. Lee, E.S. Choi, H.B. Cao, H.J. Silverstein, C.R. Wiebe, J.-G. Cheng, H.D. Zhou, Antiferromagnetic order in the pyrochlores $R_2Ge_2O_7$ (R= Er, Yb), Phys. Rev. B 92 (2015) 140407.
[28] A.M. Hallas, J. Gaudet, M.N. Wilson, T.J. Munsie, A.A. Aczel, M.B. Stone, R.S. Freitas, A.M. Arevalo-Lopez, J.P. Attfield, M. Tachibana, C.R. Wiebe, G.M. Luke, B.D. Gaulin, XY antiferromagnetic ground state in the effective S= 1/2 pyrochlore $Yb_2Ge_2O_7$, Phys. Rev. B 93 (2016) 104405.
[29] X. Li, Y.Q. Cai, Q. Cui, C.J. Lin, Z.L. Dun, K. Matsubayashi, Y. Uwatoko, Y. Sato, T. Kawae, S.J. Lv, C.Q. Jin, J.-S. Zhou, J.B. Goodenough, H.D. Zhou, J.-G. Cheng, Long-range magnetic order in the Heisenberg pyrochlore antiferromagnets $Gd_2Ge_2O_7$ and $Gd_2Pt_2O_7$ synthesized under high pressure, Phys Rev. B 94 (2016) 214429.
[30] X. Ke, M.L. Dahlberg, E. Morosan, J.A. Fleitman, R.J. Cava, P. Schiffer, Magnetothermodynamics of the Ising antiferromagnet $Dy_2Ge_2O_7$, Phys. Rev. B 78 (2008) 104411.
[31] E. Morosan, J.A. Fleitman, Q. Huang, J.W. Lynn, Y. Chen, X. Ke, M.L. Dahlberg, P. Schiffer, C.R. Craley, R.J. Cava, Structure and magnetic properties of the $Ho_2Ge_2O_7$ pyrogermanate, Phys. Rev. B 77 (2008) 224423.
[32] L.T. Denisova, L.A. Irtyugo, Y.F. Kargin, N.V. Belousova, V.V. Beletskii, V.M. Denisov, Synthesis and high-temperature heat capacity of $Dy_2Ge_2O_7$ and $Ho_2Ge_2O_7$, Inorg. Mater. 54 (2018) 361–365.
[33] W. Hayes, R. Loudon, Scattering of Light by Crystals, Wiley, New York, 1978.
[34] P.E. Champness, Convergent beam electron diffraction, Mineral. Mag. 51 (1987) 33–48.
[35] E. Preuss, B. Krahl-Urban, R. Butz, Laue Atlas: Plotted Laue Back-Reflection Patterns of the Elements, the Compounds RX and RX2, (1974).
[36] R.F. Egerton, Electron energy-loss spectroscopy in the electron microscope, Springer Science & Business Media, 2011.
[37] S. Honglong, Z. Guling, Z. Bin, L. Minting, W. Wenzhong, A method for structure analysis of nanomaterials by electron diffraction: phase identification and unit cell determination, Microsc. Res. Techniq. 76 (2013) 641–647.
[38] A. Dias, L.A. Khalam, M.T. Sebastian, C.W.A. Paschoal, R.L. Moreira, Chemical substitution in $Ba(RE_{1/2}Nb_{1/2})O_3$ (RE= La, Nd, Sm, Gd, Tb, and Y) microwave ceramics and its influence on the crystal structure and phonon modes, Chem. Mater. 18 (2006) 214–220.
[39] A. Dias, L.A. Khalam, M.T. Sebastian, M.M. Lage, F.M. Matinaga, R.L. Moreira, Raman scattering and infrared spectroscopy of chemically substituted Sr_2LnTaO_6 (Ln= Lanthanides, Y, and In) double perovskites, Chem. Mater. 20 (2008) 5253–5259.
[40] K.P.F. Siqueira, R.L. Moreira, A. Dias, Synthesis and crystal structure of lanthanide orthoniobates studied by vibrational spectroscopy, Chem Mater. 22 (2010) 2668–2674.
[41] K.P.F. Siqueira, A. Dias, Influence of the processing conditions and chemical environment on the crystal structures and phonon modes of lanthanide orthotantalates, Dalton Trans. 40 (2011) 9454–9460.
[42] A. Dias, M.M. Lage, L.A. Khalam, M.T. Sebastian, R.L. Moreira, Vibrational spectroscopy of Ca_2LnTaO_6 (Ln= lanthanides, Y, and In) and Ca_2InNbO_6 double perovskites, Chem. Mater. 23 (2010) 14–20.
[43] K.P.F. Siqueira, R.M. Borges, E. Granado, L.M. Malard, A.M. De Paula, R.L. Moreira, A. Dias, Crystal structure of fluorite-related Ln_3SbO_7 (Ln = La–Dy) ceramics studied by synchrotron X-ray diffraction and Raman scattering, J. Solid State Chem. 203 (2013) 326–332.
[44] K.P.F. Siqueira, P.P. Lima, R.A.S. Ferreira, L.D. Carlos, E.M. Bittar, E. Granado, J.C. González, A. Abelenda, R.L. Moreira, A. Dias, Lanthanide orthoantimonate light emitters: structural, vibrational, and optical properties, Chem. Mater. 26 (2014) 6351–6360.
[45] K.P.F. Siqueira, J.C. Soares, E. Granado, E.M. Bittar, A.M. De Paula, R.L. Moreira, A. Dias, Synchrotron X-ray diffraction and Raman spectroscopy of Ln_3NbO_7 (Ln= La, Pr, Nd, Sm-Lu) ceramics obtained by molten-salt synthesis, J. Solid State Chem. 209 (2014) 63–68.
[46] K.M. Taddei, L. Sanjeewa, J.W. Kolis, A.S. Sefat, C. de la Cruz, D.M. Pajerowski, Local-Ising-type magnetic order and metamagnetism in the rare-earth pyrogermanate $Er_2Ge_2O_7$, Phys. Rev. Mater. 3 (2019) 014405.